





## Article

# Structural, Dielectric, and Mechanical Properties of High-Content Cubic Zirconia Ceramics Obtained via Solid-State Synthesis

Sholpan G. Giniyatova <sup>1</sup>, Artem L. Kozlovskiy <sup>1,2,\*</sup> , Rafael I. Shakirzyanov <sup>1</sup>, Natalia O. Volodina <sup>1</sup> ,  
Dmitriy I. Shlimas <sup>1,3</sup>  and Daryn B. Borgekov <sup>1,3</sup> 

<sup>1</sup> Engineering Profile Laboratory, L.N. Gumilyov Eurasian National University, Astana 010008, Kazakhstan; giniyatova\_shg@enu.kz (S.G.G.); halfraf@mail.ru (R.I.S.)

<sup>2</sup> Department of General Physics, Satbayev University, Almaty 050032, Kazakhstan

<sup>3</sup> Laboratory of Solid State Physics, The Institute of Nuclear Physics, Almaty 050032, Kazakhstan

\* Correspondence: kozlovskiy.a@inp.kz; Tel./Fax: +7-702-441-3368

**Abstract:** In this work, the structural, electrical, and mechanical properties and phase composition of high-content cubic zirconium oxide ceramics stabilized with Ca were investigated. The novelty of this work lies in evaluating the potential use of porous ceramics obtained using calcium carbonate as a matrix for dispersed nuclear fuel. Experimental samples were prepared using solid-phase synthesis through sintering in air at 1500 °C. The X-ray diffraction method and Raman spectroscopy showed that the fraction of the cubic zirconium oxide ZrO<sub>2</sub>-c phase gradually increased as the mass concentration changed from C<sub>w</sub> = 0.00 to C<sub>w</sub> = 0.15, and the CaZrO<sub>3</sub> phase was present at concentrations of C<sub>w</sub> = 0.20 and C<sub>w</sub> = 0.25. When the phase composition was altered, significant changes occurred in the internal microstructure of the ceramics due to the processes of grain sintering and pore formation. Quantitative XRD analysis demonstrated the incorporation of Ca into the cubic structure of the ZrO<sub>2</sub>-c polymorph. Dielectric spectroscopy at low frequencies revealed that the synthesized ceramics had a dielectric constant of 16.8–22 with a low dielectric loss of ~ 0.005. The microhardness value at a load of 200 kgf (HV0.2) of the obtained samples varied between 5 and 12 GPa and depended on the internal microstructure and phase composition. The obtained results clearly indicate that the mechanical and electrical properties and phase composition of synthesized ceramics make them suitable as a matrix for dispersed nuclear fuels.

**Keywords:** stabilized zirconia ceramics; dielectric permittivity; polymorphic transformations; microstructure; dispersed fuel



**Citation:** Giniyatova, S.G.; Kozlovskiy, A.L.; Shakirzyanov, R.I.; Volodina, N.O.; Shlimas, D.I.; Borgekov, D.B. Structural, Dielectric, and Mechanical Properties of High-Content Cubic Zirconia Ceramics Obtained via Solid-State Synthesis. *Appl. Sci.* **2023**, *13*, 10989. <https://doi.org/10.3390/app131910989>

Academic Editor: Fernando Rubio-Marcos

Received: 14 September 2023

Revised: 1 October 2023

Accepted: 4 October 2023

Published: 5 October 2023



**Copyright:** © 2023 by the authors. Licensee MDPI, Basel, Switzerland. This article is an open access article distributed under the terms and conditions of the Creative Commons Attribution (CC BY) license (<https://creativecommons.org/licenses/by/4.0/>).

## 1. Introduction

At present, great efforts are aimed at making nuclear power safer for the environment. One important direction of this research is the use of oxide and nitride inert matrices for nuclear fuel. In this type of fuel, uranium is substituted with elements that do not create actinides when bombarded by neutrons. Thus, it will be possible to reduce the amount of additional plutonium generated through the burning of conventional uranium dioxide nuclear fuel [1]. The study of inert matrices for nuclear fuel is a current focus due to various reasons, such as the high energy potential of plutonium, the possibility of processing large stockpiles of weapons-grade plutonium, and the fact that transuranic elements can significantly increase the radiotoxicity of conventional spent fuel beyond several hundred years.

Inert matrices represent conventional ceramics, in which actinide oxide globules are uniformly spread. These materials must act as a mechanical support, withstanding deformations caused by fission and heat dissipation. For this reason, the ceramics being developed must have excellent mechanical properties such as strength, crack resistance,

and hardness. Besides excellent mechanical properties, good thermal conductivity and a low expansion coefficients must be realized too. Also, these ceramics are exposed to a significant amount of radiation caused by fission products. They must be able to sustain damage of up to 10,000 dpa without significant deterioration (including secondary phase formation and transmutation effects) [2]. A review of the literature on the properties of ceramic materials shows the most suitable candidates for the role of inert matrices, such as MgO, CeO<sub>2</sub>, ZrO<sub>2</sub>, and the nitrides ZrN and CeN [3].

Zirconium oxide is a great choice for the inert matrix of dispersed nuclear fuel due to its high melting point of 2700 °C, low neutron absorption cross-section, and outstanding mechanical properties (strength, hardness, and fracture toughness) [4]. To obtain zirconia ceramics, different methods such as solid-state sintering [5], hydrothermal methods [6], physical vapor deposition [7], and anodization [8] can be used. Pure zirconia has a monoclinic stable structure at ambient temperature, which changes to a tetragonal phase upon heating (1170–2370 °C) and to a cubic structure at higher temperatures (2370–2680 °C) [9]. The tetragonal-to-monoclinic transition is martensitic and leads to a volume expansion of around 4%. Since this expansion causes significant internal stresses that can induce cracking and even component failure upon cooling after sintering, pure zirconia's applications as an advanced ceramic have been severely constrained [10].

To overcome problems with ceramic cracking and make industrial applications possible, the high-temperature tetragonal or cubic phases must be stabilized. The formation of these highly symmetrical phases can be achieved by doping the oxide with cations with an ionic radius close to that of tetravalent zirconium, such as Mg<sup>2+</sup>, Ca<sup>2+</sup>, Y<sup>3+</sup>, or Ce<sup>4+</sup>. The stability of the cubic and tetragonal phases may both be controlled by the quantity of doping oxide supplied [11].

Recently, it was discovered that calcia-doped zirconia ceramics display the same phase transformation features and hardness properties as yttria-doped zirconia ceramics, but can be made at a lower cost and in higher quantities owing to the accessibility of calcium precursors compared to yttrium [12]. In addition, calcium doping produces twice as many vacancies in zirconium dioxide as yttrium does, which leads to a higher ionic conductivity of Ca-doped ZrO<sub>2</sub> than Y-doped ZrO<sub>2</sub> [13]. Therefore, Ca-stabilized ZrO<sub>2</sub> has been considered for use as an electrolyte in solid oxide fuel cells and oxygen detectors [14,15].

Previous studies performed on 16 mol% calcium-doped zirconia showed that the sintering temperature is the primary factor influencing the characteristics of the obtained ceramics. Above 1000 °C, a solid-state interaction between calcium oxide and zirconium oxide occurred, and at 1400 °C, a completely stable cubic phase (97%) formed. Using TG/DSC analysis, the authors verified that calcium-stabilized zirconia is stable at high temperatures; thus, it is especially useful for high-temperature applications [16]. This feature can be advantageous to tetragonal-stabilized zirconia ceramics because of the absence of the reversible phase transformation in high-content cubic zirconia ceramics.

As is known, the most widespread method of producing functional ceramics is solid-phase synthesis using oxides, which includes co-milling of the initial reagents, pressing, and sintering [17,18]. However, other reagents, such as carbonates, are often used in ceramic technology to control shrinkage and pore formation [19–21]. To unambiguously evaluate the suitability of ceramics for inert matrices, high-cost experiments with the irradiation of heavy ions in ion beam accelerators can be performed [22]. Prior to this test, standard material characterization must be performed. The purpose of this paper is to investigate the mechanical and electrical properties and structural features of high-content cubic zirconia ceramics obtained via solid-state sintering. Through a detailed analysis of how the doping of zirconium oxide with CaCO<sub>3</sub> affects the lattice parameters, phase composition, particle size, microhardness, and dielectric properties of sintered ceramics, a preliminary estimation of its applicability in nuclear power as inert matrices was performed.

## 2. Experimental Section

The experimental samples were synthesized via solid-phase sintering. The initial components were zirconium oxide (Sigma Aldrich, Burlington, MA, USA, CAS Registry number 1314-23-4, particle size < 5  $\mu\text{m}$ , density 5.89  $\text{g}/\text{cm}^3$ , purity  $\geq 99.99\%$ ) and calcium carbonate (Sigma Aldrich, Burlington, MA, USA, CAS Registry Number 471-34-1, particle size < 5  $\mu\text{m}$ , density 2.93  $\text{g}/\text{cm}^3$ , purity  $\geq 99.99\%$ ). In the initial mixture, the concentrations of  $\text{CaCO}_3$  (dopant) expressed through the weight fraction of  $C_w$  were 0.05, 0.10, 0.15, 0.20, and 0.25. In the first step, the initial mixture was homogenized via dry milling. Prior to the milling process, the initial powders were weighed using high-precision scales according to the weight fraction. For homogenization, the planetary mill PULVERISETTE 6 classic line (Fritsch International, Idar-Oberstein, Germany) with tungsten carbide balls was used. Dry milling of the charge was carried out for 30 min at 250 rpm; the ratio of balls to mixture was 2:1. In the second step, the resulting homogenized powder was mixed with the binder of an aqueous solution of polyvinyl alcohol (JSC EuroChem, Kovdor, Russia, 16/1 grade, CAS Registry Number 9002-89-5, molecular weight 31,000–50,000) in the required ratio (about 1 wt.% of the polyvinyl alcohol in the dry residue). In the third step, green pellets from pressed powders were formed via pressing. A hydraulic press and a stainless steel mold were used to produce green pellets of the resulting powder in the form of tablets with a thickness of  $\sim 1$  mm and a diameter of 12.1 mm by applying a pressure of  $\sim 200$  MPa. In the final step, the samples were sintered in the air at 1500  $^\circ\text{C}$  for 5 h in a muffle furnace using a corundum crucible.

The obtained ceramic tablets were investigated via X-ray powder diffraction (XRD) using a D8 Advance Eco diffractometer (Bruker GmbH, Mannheim, Germany), Raman spectroscopy using an Enspectr M532 spectrometer (Spectr-M LLC, Chernogolovka, Russia), and dielectric spectroscopy using a HIOKI IM3533 LCR meter (HIOKI E.E. Corporation, Ueda, Japan). To perform dielectric measurements, silver paste was applied to both sides of the tablet surface to create a plain capacitor structure. Micrographs were taken on cross-sections of the tablets using a Hitachi TM 3030 scanning electron microscope (SEM) (Hitachi Ltd., Tokyo, Japan) at an accelerating voltage of 15 kV. Elemental analysis and elemental mapping were performed using a Quantax 70 unit (Bruker GmbH, Mannheim, Germany). The morphological parameters (the grains' size and distribution) were evaluated using ImageJ software 1.54f. Before grain size calculation, the digital images obtained via SEM were adjusted to obtain a clear, high-contrast view of the grains. After that, automatic and manual defining of the grain outlines with calculation of the Feret diameter were carried out. The microhardness of the obtained ceramics was determined using the Vickers method with a diamond indenter on a METKON Durolin-M microhardness tester (Metkon Instruments Inc., Bursa, Turkey) under a load of 0.2 kgf at a dwell time of 10 s. Before the hardness test, the surface of the tablets was gently ground and polished according to the procedures in DIN EN ISO 6507-2:2018 [23] and ISO 14705:2016 [24].

## 3. Results and Discussion

The physical properties and structural characteristics of oxide ceramics are strongly dependent on their phase composition [25]. For this reason, the identification of the phase composition of the obtained samples via powder X-ray diffraction and Raman spectroscopy was conducted. The X-ray powder diffractograms for the synthesized ceramics are shown in Figure 1. Phase analysis showed the presence of three phases in the samples:  $\text{ZrO}_2\text{-m}$  (zirconium oxide monoclinic cell, space group P21/c, COD 04-004-4339),  $\text{ZrO}_2\text{-c}$  (zirconium oxide cubic cell, space group Fm-3m, COD 04-002-8314), and  $\text{CaZrO}_3$  (calcium zirconate orthorhombic cell, space group Pcmn, PDF 00-035-0790). Quantitative analysis of the diffractograms was conducted via the Rietveld method using Profex 5.0.2 software [26]. The phase analysis revealed that the undoped ceramics had only the monoclinic  $\text{ZrO}_2\text{-m}$  phase. With increasing dopant concentrations up to  $C_w = 0.05\text{--}0.15$ , two zirconium oxide phases were present in the ceramics: monoclinic  $\text{ZrO}_2\text{-m}$  and cubic  $\text{ZrO}_2\text{-c}$ . With a further increase

in  $\text{CaCO}_3$  concentration, no monoclinic phase was found and the phase composition was represented by the  $\text{ZrO}_2$ -c phase together with the perovskite  $\text{CaZrO}_3$  phase.

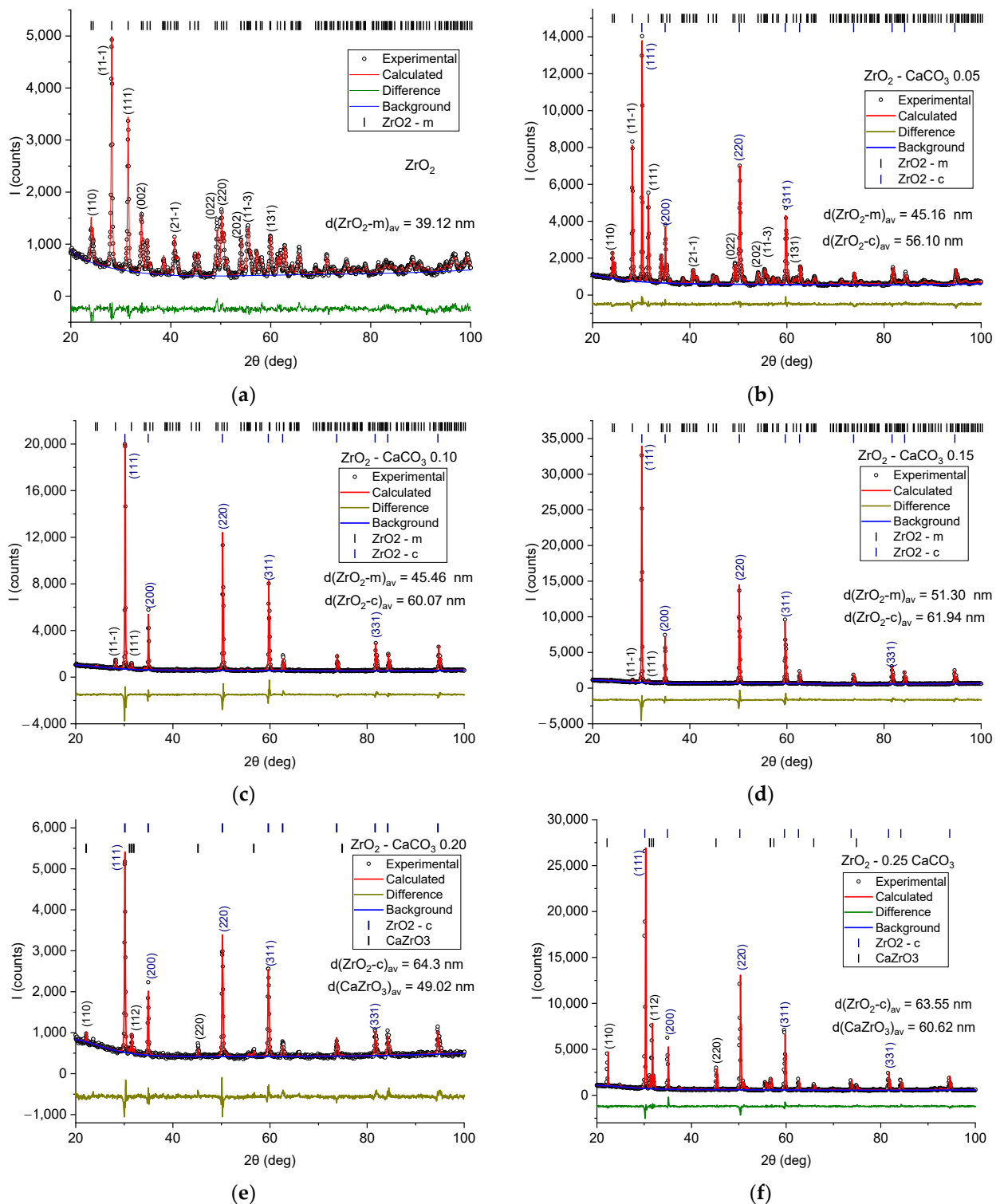


**Figure 1.** Powder diffractograms of the obtained samples. (a) pristine; (b)  $C_w = 0.05$ ; (c)  $C_w = 0.10$ ; (d)  $C_w = 0.15$ ; (e)  $C_w = 0.20$ ; (f)  $C_w = 0.25$ .

The sintering of the  $\text{ZrO}_2$ -m charge with a small amount of dopant containing  $\text{Ca}^{2+}$  ions leads to the replacement of  $\text{Zr}^{4+}$  ions by calcium and the formation of oxygen vacancies [27]. This substitution is the driving force for stabilizing the  $\text{ZrO}_2$ -c phase and

suppressing the martensitic transition upon cooling to room temperature [28]. When the dopant concentration was increased to 0.20, the  $\text{CaZrO}_3$  phase was formed. It can be argued that at a concentration of 0.20, the limit at which  $\text{Ca}^{2+}$  ions can enter the crystal lattice of the  $\text{ZrO}_2$ -c phase was reached. The formation of cubic-phase  $\text{ZrO}_2$ -c with  $\text{CaZrO}_3$  at concentrations of 0.20 and 0.25 agrees with the obtained phase diagrams for the  $\text{CaO}$ - $\text{ZrO}_2$  system [29,30]. Despite using calcium carbonate as the initial reagent, the annealing process is presumed to cause the decomposition of  $\text{CaCO}_3 \rightarrow \text{CaO} + \text{CO}_2$  (decomposition temperature  $\sim 1000^\circ\text{C}$ ), followed by the reaction  $\text{CaO} + \text{ZrO}_2 \rightarrow \text{CaZrO}_3$ . As a result, the experimental data align well with the phase diagrams.

The results of the calculated values of the lattice parameters for the measured diffractograms are given in Tables 1 and 2. The observed increase in the lattice parameter and volume in the cubic phase suggests that the incorporation of  $\text{Ca}^{2+}$  ions, which have a larger ionic radius, into the  $\text{ZrO}_2$ -m structure leads to two significant outcomes. Firstly, it induces the transition of the monoclinic phase into the cubic phase. Secondly, it causes the expansion of the cubic unit cell. In the case of the  $\text{ZrO}_2$ -m phase, the unit cell volume decreases with increasing dopant concentration owing to the decrease in parameters  $a$  and  $b$ . The highest values of the unit cell volume and parameters  $a$  and  $b$  for the undoped sample can be attributed to the tensile stresses developed after cooling. To confirm this hypothesis, the Williamson–Hall method was applied to an undoped sample to determine the type of stress (compressive or tensile) from an analysis of the diffractogram peaks. [31]. The FWHM (Full Width at Half Maximum) and the peak center of the most prominent reflections were determined using Profex 5.0.2 software. Figure 2a shows that the approximation line has a positive slope, indicating tensile stresses. Thus, it can be stated that the increased value of the lattice parameters in the undoped ceramics is due to tensile stresses. These stresses arise during cooling, when a transition from the tetragonal phase to the monoclinic phase occurs.

**Table 1.** Results of quantitative analysis of diffractograms via the Rietveld method for ceramics with monoclinic and cubic phases.

Sample	Monoclinic Phase					Cubic Phase			
	$a, \text{Å}$	$b, \text{Å}$	$c, \text{Å}$	$\beta, ^\circ$	$V, \text{Å}^3$	XRD Density, $\text{g/cm}^3$	$a, \text{Å}$	$V, \text{Å}^3$	XRD Density, $\text{g/cm}^3$
$\text{ZrO}_2$	5.1509	5.2060	5.3215	99.22	140.855	5.810	-	-	-
0.05	5.1537	5.2044	5.3191	99.22	140.825	5.811	5.1272	134.785	6.072
0.10	5.1468	5.1973	5.3199	99.21	140.469	5.826	5.1292	134.943	6.014
0.15	5.1367	5.1993	5.3264	99.21	140.420	5.828	5.1381	135.646	6.033

**Table 2.** Results of quantitative analysis of diffractograms via the Rietveld method for ceramics with perovskite and cubic phases.

Sample	Cubic Phase			Perovskite Phase				
	$a, \text{Å}$	$V, \text{Å}^3$	XRD Density, $\text{g/cm}^3$	$a, \text{Å}$	$b, \text{Å}$	$c, \text{Å}$	$V, \text{Å}^3$	XRD Density, $\text{g/cm}^3$
0.20	5.13707	135.565	6.037	5.6001	5.7526	8.0157	258.2269	4.612
0.25	5.1411	135.884	6.022	5.5940	5.7561	8.0174	258.1573	4.613

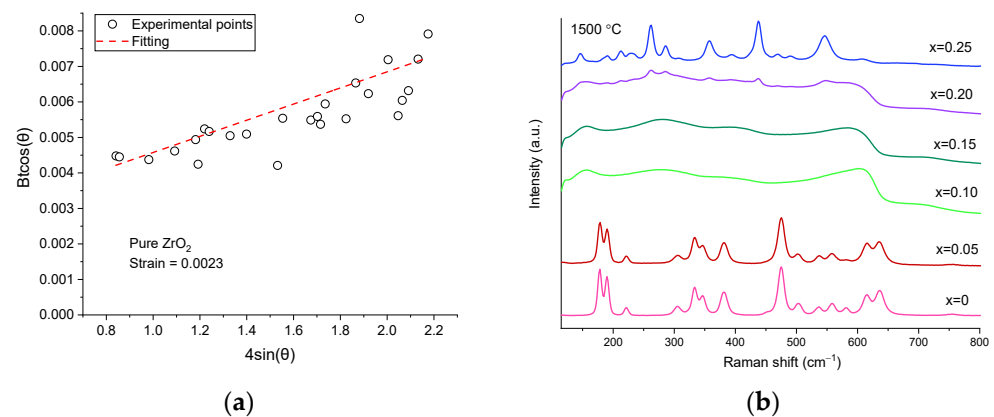


**Figure 2.** W-H dependence for undoped  $\text{ZrO}_2$  (a) and Raman spectra of synthesized ceramics (b).

The average crystalline size was calculated using the Debye–Scherer equation for all samples. The main characteristic peaks of each phase were also fitted using Profex 5.0.2 software. The results of this calculation are presented in Figure 1. The lowest crystalline size for an undoped sample can be explained by tensile stresses in the crystal structure. It is observed that with increasing Ca content in sintered ceramics, the average crystallites become larger. The possible reason for this fact is that in stabilized cubic zirconia, during the cooling  $t \rightarrow m$  transformation, significant distortion of the crystal lattice does not occur. This leads to the relaxation of tensile stresses and increases the crystallite size.

Table 3 lists the statistical parameters of the Rietveld refinement and phase composition of the obtained ceramics. The parameters R-factor ( $R_{\text{exp}}$ ,  $R_{\text{wp}}$ ), goodness of fit (GOF), and standard deviation  $\chi^2$  exhibit relatively low values, indicating the fitting results' reliability. These low values imply a small difference between the experimental and calculated data, thus affirming the accuracy of the fitting process. Based on the evaluation of the phase composition and lattice parameters of the resulting ceramics, it can be concluded that an increase in  $\text{CaCO}_3$  concentration leads to the following changes in the phase composition:  $\text{ZrO}_2\text{-m}$  transitions to  $\text{ZrO}_2\text{-m} + \text{ZrO}_2\text{-c}$  with the substitution of  $\text{Zr}^{4+}$  by  $\text{Ca}^{2+}$  ions in the range of  $C_w = 0.05\text{--}0.15$ ;  $\text{ZrO}_2\text{-c}$  coexists with  $\text{CaZrO}_3$ , reaching the substitution limit with the separation of the second phase. Moreover, by varying the dopant concentration from 0 to 0.10, it is possible to obtain partially stabilized zirconium oxide ceramics. At a concentration of 0.15, fully stabilized ceramics are formed. In the concentration range of 0.20 to 0.25, partially stabilized zirconia ceramics with a fraction of  $\text{CaZrO}_3$  are obtained.

**Table 3.** Statistical parameters of Rietveld refinement and phase composition obtained from the analysis of diffractograms.

Sample	$R_{\text{exp}}$	$R_{\text{wp}}$	GOF	$\chi^2$	Phase Composition, %		
					$\text{ZrO}_2\text{-m}$	$\text{ZrO}_2\text{-c}$	$\text{CaZrO}_3$
$\text{ZrO}_2$	4.02	6.07	1.51	2.28	100	0	0
0.05	3.45	4.55	1.32	1.74	63.45	36.55	0
0.10	3.77	6.36	1.69	2.85	8.75	91.25	0
0.15	3.63	5.85	1.61	2.60	2.82	97.18	0
0.20	4.32	6.78	1.57	2.46	0	88.60	11.40
0.25	3.69	5.51	1.49	2.23	0	64.58	34.42

Since the set of peaks in the powder diffractogram of the tetragonal zirconium oxide phase closely resembled those of the cubic  $\text{ZrO}_2\text{-c}$  phase, Raman spectroscopy (Figure 2b) was employed to clarify the phase composition of the synthesized ceramics. In the case of pure zirconium oxide sintered at  $1500\text{ }^\circ\text{C}$ , fourteen active modes were observed: seven  $A_g$  ( $178, 190, 306, 346, 475, 558, \text{ and } 636\text{ cm}^{-1}$ ), six  $B_g$  ( $221, 333, 381, 503, 536, \text{ and } 615\text{ cm}^{-1}$ ), characteristic of the monoclinic phase [32], and a peak at  $581\text{ cm}^{-1}$ , which disappeared at a

Ca concentration of 0.05. The spectra of the samples with Ca concentrations of 0.10 and 0.15 showed only three very broad peaks at 156, 277, and 608  $\text{cm}^{-1}$ , associated with the cubic phase of the fluorite structure ( $\text{O}_h^5$ ,  $\text{F}_{m-3m}$ ) [16]. At a Ca concentration of 0.20, the broad peaks of the cubic phase were still pronounced, but new sharp peaks also began to appear. Finally, for a Ca concentration of 0.25, Raman modes were observed at 146, 190, 212, 230, 262, 286, 309, 358, 438, 470, and 546  $\text{cm}^{-1}$ , indicating the formation of orthorhombic perovskite-phase  $\text{CaZrO}_3$  [33]. Notably, the peak at 610  $\text{cm}^{-1}$  indicated the cubic phase of zirconium oxide. Thus, the results of the powder diffractogram analysis were enhanced using Raman spectroscopy.

Figure 3 shows microphotographs of the cross-sections of the obtained ceramics. The microstructure of the undoped sample (Figure 3a) was characterized by the presence of well-defined grains with a large number of faces, a pronounced intergrain boundary, and the presence of intergrain pores. The mentioned grain shape is largely characteristic of crystallites with a monoclinic crystal lattice. When the dopant was introduced at a concentration of  $C_w = 0.05$  (Figure 3b), significant changes in the microstructure occurred. In addition to grains with sizes of 2–3  $\mu\text{m}$ , smaller grains and larger grains with sizes of 6–8  $\mu\text{m}$  were formed. Upon further increasing the proportion of  $\text{CaCO}_3$  in the charge, the microstructure of the synthesized ceramics (Figure 3c–f) exhibited grains with relatively complex shapes. This complexity arose from the sintering process, resulting in the fusion of individual grains. Additionally, there was a reduced number of intergranular boundaries, and the presence of intergrain pores was observed.

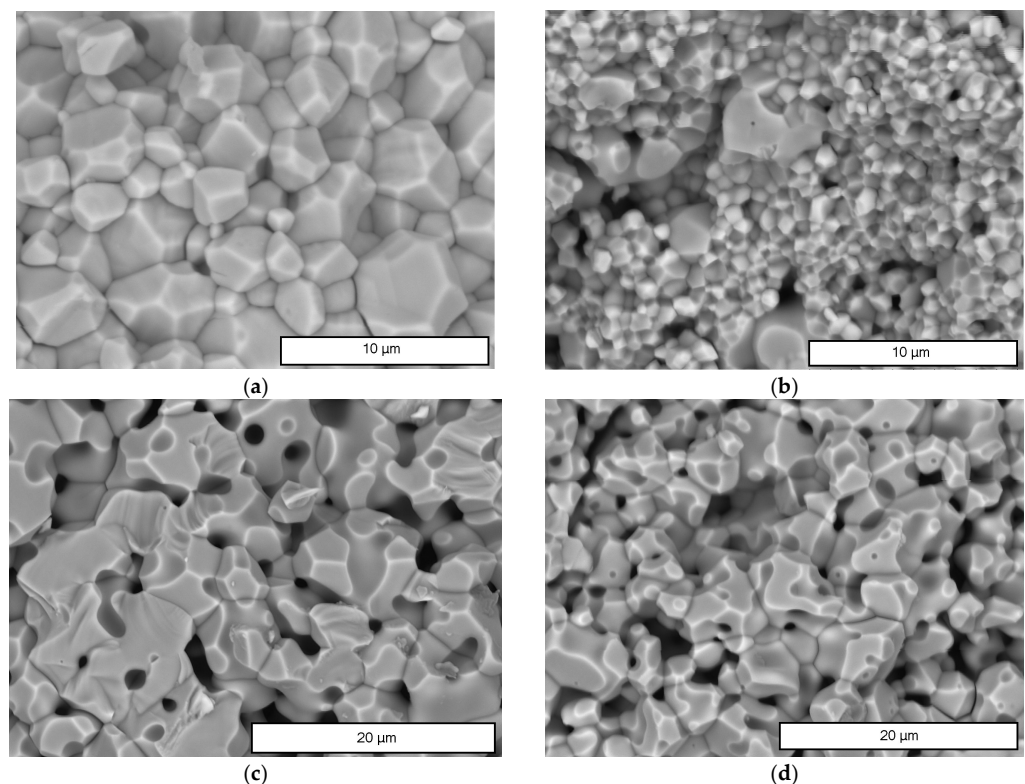
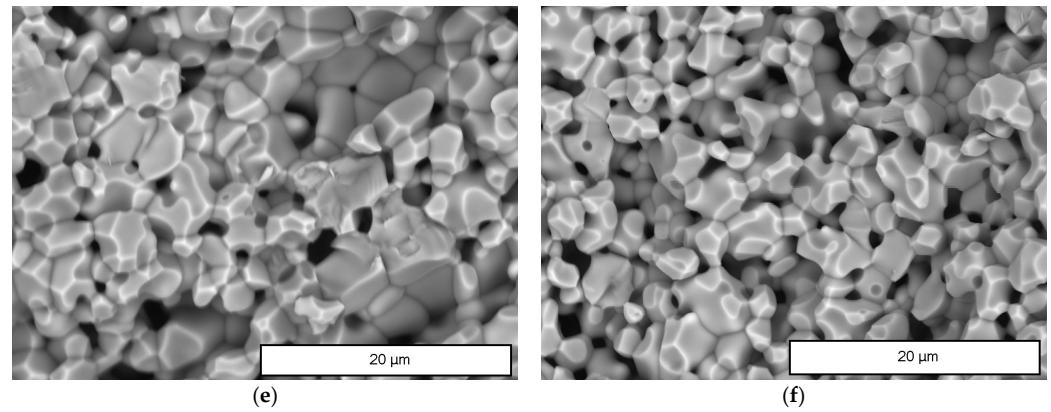
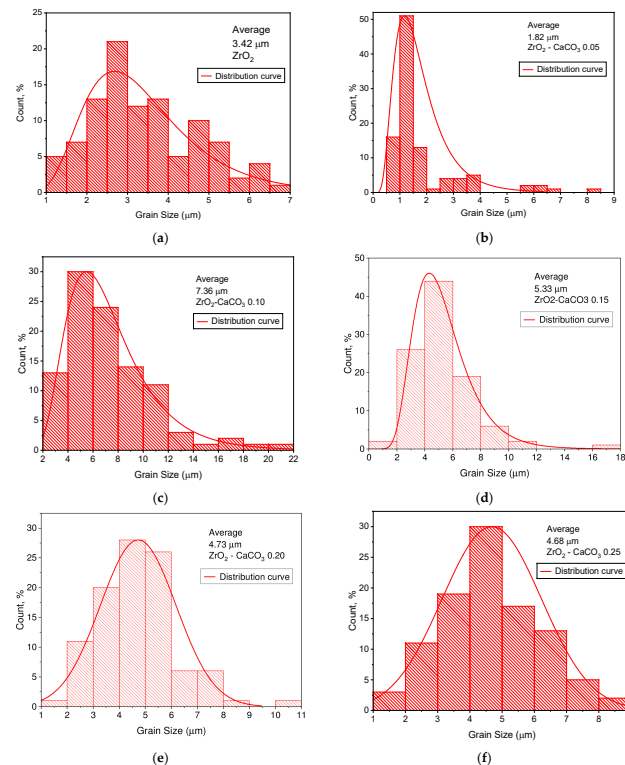


Figure 3. Cont.



**Figure 3.** SEM micrographs of synthesized ceramics (a) pristine; (b)  $C_w = 0.05$ ; (c)  $C_w = 0.10$ ; (d)  $C_w = 0.15$ ; (e)  $C_w = 0.20$ ; (f)  $C_w = 0.25$ .

For a more detailed analysis of the microstructure of the synthesized samples, the grain size distribution in the ceramics was evaluated using ImageJ software 1.54f [34]. For the set of statistics, the sizes of 100 grains were determined from the SEM micrographs. The results of the analysis are presented as histograms in Figure 4. As can be seen from the figure, the average grain size decreased at  $C_w = 0.05$  from 3.42 to 1.82  $\mu\text{m}$ . At a dopant concentration of 0.10, the average size reached a maximum value of 7.36  $\mu\text{m}$  and decreased again with increasing concentrations of 0.15, 0.20, and 0.25 to values of 5.33, 4.73, and 4.68  $\mu\text{m}$ , respectively. In the undoped sample (Figure 4a), a broad grain size distribution was observed with a peak at 2.5–3  $\mu\text{m}$ , comprising no more than 22% of the grains. However, at low dopant concentrations ( $C_w = 0.05$ , Figure 4b), the grain size distribution became narrower, with a peak in the range of 1–1.5  $\mu\text{m}$ . An important observation is the presence of grains with sizes that are twice the average grain size. This indicates the initiation of grain growth, likely resulting from phase transformations during the diffusion process.

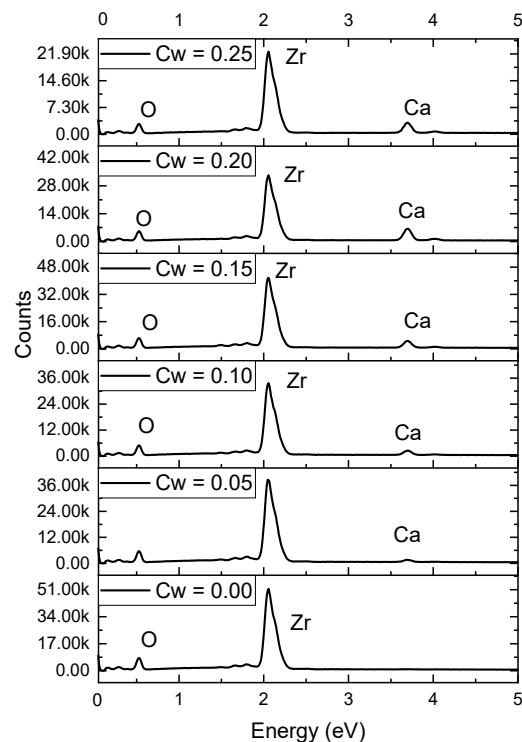


**Figure 4.** Histograms of grain size distribution (a) pristine; (b)  $C_w = 0.05$ ; (c)  $C_w = 0.10$ ; (d)  $C_w = 0.15$ ; (e)  $C_w = 0.20$ ; (f)  $C_w = 0.25$ .



Samples with dopant concentrations of  $C_w = 0.10$  and  $0.15$  (Figure 4c,d) exhibited large ranges of grains size, spanning from 0 to  $22\ \mu\text{m}$ . This indicates the occurrence of intensive processes of grain coalescence and coarsening during annealing [35]. These samples were characterized by the highest values of the fraction of the cubic phase (Table 3), signifying the decisive contribution of phase transformations during atomic diffusion to grain growth [36]. However, with increasing concentration, a decrease in the grain size range and average grain size were observed. This can be attributed to the large concentration of  $\text{CO}_2$  gas released during annealing, which forms pores. The presence of pores is a critical factor in the further densification of ceramics due to the grain growth [27]. For this reason, for concentrations of  $0.20$  and  $0.25$  (Figure 4e,f), despite the intense coalescence and expansion of grains, the average grain size and distribution range decreased. It can also be argued that the  $\text{CaCO}_3$  in the charge is a pore-forming agent and significantly affects the microstructure of zirconia ceramics.

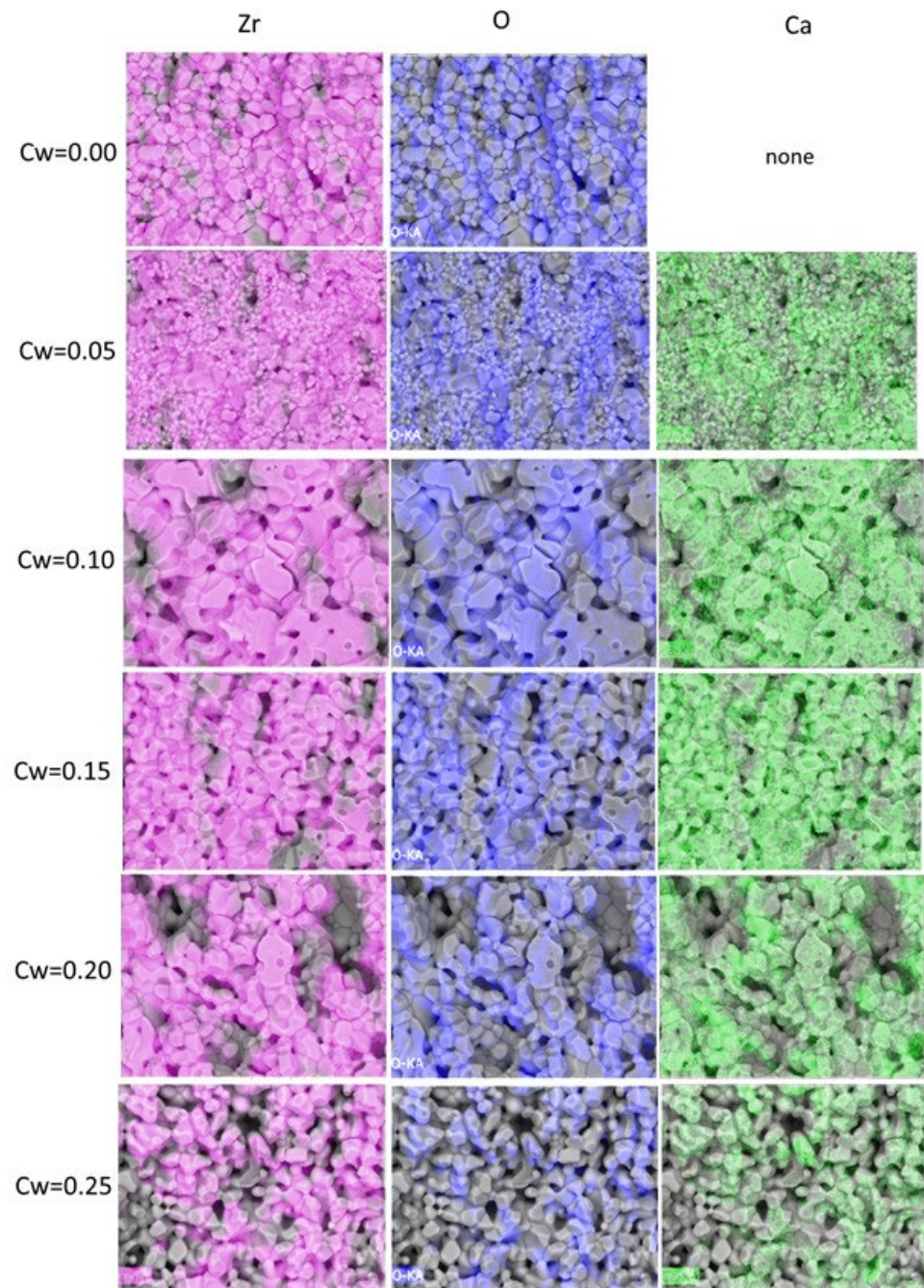
Figure 5 shows the spectra of the energy-dispersive analysis of the obtained ceramics. The spectra suggest that the synthesized samples contained only Ca, Zr, and O. With increasing dopant concentration, the intensity of the peak related to Ca increased, indicating an increase in the concentration of this element in the ceramic composition. The chemical composition of the obtained samples is shown in Table 4. The analysis of the peaks using Quantax 75 software over the scan area shown in Figure 6 demonstrates that the atomic percentage of Ca increased with increasing  $C_w$ . The discrepancy between the atomic percentages and stoichiometric formulas can be explained by the large degree of roughness of the cross-sections. This roughness makes it difficult to detect X-ray photons, which can change the atomic composition from stoichiometric. Elemental mapping of the cross-section of the ceramic sample showed that oxygen and zirconium ions were uniformly distributed over the ceramic surface. However, for the sample with a concentration  $C_w = 0.05$ , it can be observed that Ca ions were distributed predominantly in large grains. Considering the results of the powder diffractogram analysis, it can be concluded that the small grains were predominantly composed of monoclinic phases. In the case of ceramics with high dopant concentrations, the non-uniform distribution is due to the formation of the  $\text{CaZrO}_3$  phase, which contains more Ca than the substituted  $\text{ZrO}_2$ -c phase.



**Figure 5.** Energy-dispersive analysis spectra for synthesized ceramic samples.

**Table 4.** Results of surface chemical composition analysis using the EDX method.

$C_w$	O Concentration, at. %	Zr Concentration, at. %	Ca Concentration, at. %
0.00	54.39	45.61	-
0.05	54.85	43.97	1.17
0.10	55.02	40.24	4.74
0.15	58.78	34.83	6.39
0.20	60.40	31.17	8.43
0.25	58.46	28.07	13.47

**Figure 6.** Elemental mapping of cross-sections of fabricated specimens.

The frequency dependences of the dielectric permittivities of the synthesized ceramics are shown in Figure 7a. As is evident from the figure, the dielectric constant remains nearly constant across the frequency range of 200–200 kHz, suggesting the absence of relaxation

processes in the ceramics, unlike, for example, in ferrite ceramics like  $\text{NiFe}_2\text{O}_4$  [37–40]. Generally, the dielectric properties of ceramics depend on electronic polarization, ionic polarization, relaxation, and resonance. Low-frequency relaxation in oxide ceramics with transition elements or ions of different valences can occur in accordance with Koop's theory, which considers ceramic to be a nonhomogeneous medium with intergranular boundaries and crystalline grains with different dielectric properties [17,41]. In such a medium, there is a possibility of the Maxwell–Wagner polarization mechanism occurring between poorly conducting intergranular interfaces and well-conducting crystalline grains. This was not observed in the obtained samples, which suggests a small difference in the dielectric properties of the structural units of the synthesized zirconium ceramics (intergranular boundaries, grains, and pores). As will be shown later, the variation in the dielectric permittivity is related to the porosity of the samples and phase composition of the ceramics. Figure 7b illustrates the frequency dependence of the dielectric loss  $\tan \delta$ , which demonstrates how much of the energy of an electric sinusoidal wave is transferred to heat during the repolarization processes. Zirconia ceramics are considered to be high-Q dielectric materials for microwave application [42]. The low losses can be attributed to the presence of only losses associated with phonon vibrations in the crystal structure of high-density homogeneous ceramics, and these losses can reach values of  $5 \cdot 10^{-3}$  or even  $6 \cdot 10^{-4}$  [43]. If dielectric monocrystal or polycrystal (ceramics) is free from structural defects, impurities, porosity, and microcracks, only intrinsic loss mechanisms contribute to the value of  $\tan \delta$ . The measurement results show that the lowest losses in the larger region of the frequency spectrum were characterized by the sample without doping (0.0025–0.005). When  $C_w$  was increased to 0.05, the value of  $\tan \delta$  increased by a factor of  $\sim 3$  in the low-frequency region and decreased rapidly with increasing frequency. This behavior can be attributed to the pronounced polydispersed grain size distribution in ceramics and the presence of a large percentage of small-sized grains. In this case, the surface fraction of atoms increases, which increases the number of unsaturated chemical bonds. These unsaturated bonds can be considered defects in the crystal lattice that can anchor electrical dipoles and interfere with the polarization process. For the other samples, the dielectric losses were 0.005–0.0075 in the investigated frequency range. It can be concluded that the main mechanisms of dielectric losses in the obtained ceramics are electronic polarization and ionic polarization.

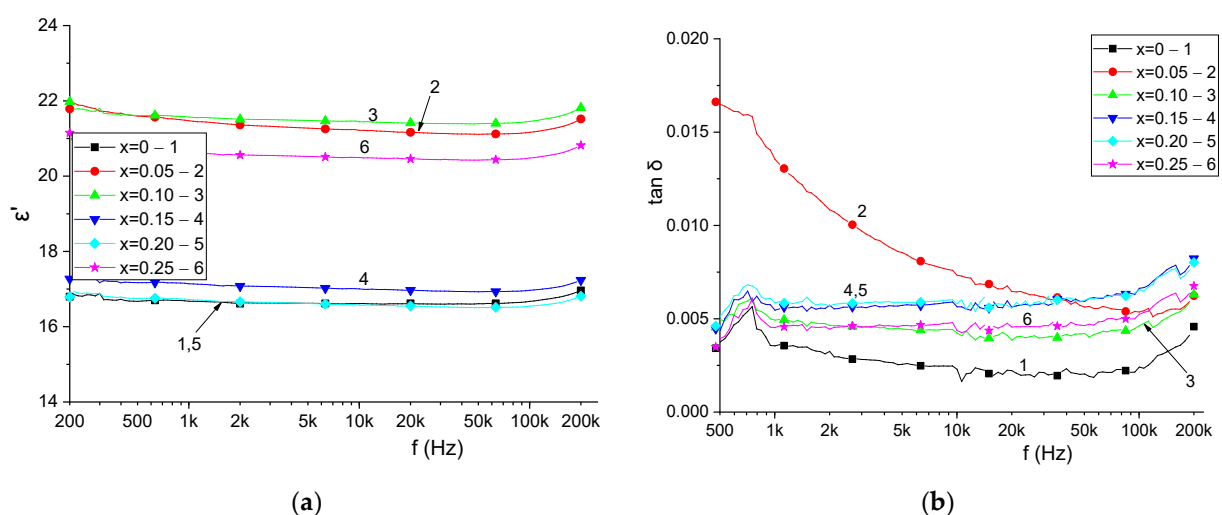


**Figure 7.** Frequency dependences of dielectric permittivity (a) and loss tangent (b) for the obtained ceramics.

To determine the reasons for the change in the dielectric constant when the dopant concentration is increased, the following factors should be considered: the porosity of the ceramics, the phase composition, and the influence of the dopant element on polarizability.

Determining the porosity of ceramics without using techniques that utilize gases or liquids requires knowledge of the density of the material. In the case of the samples studied in this work, an accurate estimation of the theoretical density is difficult because most samples are multiphase, and, as shown in the X-ray diffraction studies, the density of the phases can vary significantly (Table 2). The apparent density of the sintered tablets was determined by measuring their geometric parameters and weights. Figure 8a shows the change in the dielectric constant and apparent density as a function of the dopant concentration. Up to a concentration of  $C_w = 0.20$ , the change in the dielectric permittivity generally coincides with the change in the apparent density. The dielectric constant of the undoped sample was lower than that of the ceramics studied herein (24 vs. 16.4) [44]. This can be explained by the presence of martensitic phase transitions  $ZrO_2\text{-}m \rightarrow ZrO_2\text{-}t$  (1170 °C) and  $t \rightarrow m$ , after which mechanical stresses are formed in the undoped sample, leading to the appearance of internal microcracks that increase the porosity. This can also be observed when measuring the apparent density, which is 4.75 g/cm<sup>3</sup> versus the theoretical density of 5.8 g/cm<sup>3</sup> for the monoclinic zirconium oxide. The decrease in the apparent density of the doped ceramics is due to the increase in the number of pores in the ceramics with higher calcium carbonate concentration in the charge. The maximum apparent density was observed for ceramics with a dopant concentration of  $C_w = 0.05$ , which can be explained by the small number of pores that are formed by the release of CO<sub>2</sub> gas as well as by the peculiarities of the microstructure, in which small grains are densely packed. With a further decrease in the apparent density of ceramics with  $C_w = 0.10$ , the dielectric constant does not decrease, which may be due to the increase in the fraction of the cubic phase. In this case, as stated earlier, the cubic structure, which has a smaller crystal cell volume, is stabilized. According to the Clausius–Mossotti equation, the dielectric permittivity of the crystals is related to the polarizability and unit cell volume as follows [45]:

$$\frac{\epsilon' - 1}{\epsilon' + 2} = \frac{\alpha}{3V\epsilon_0} \quad (1)$$

where  $\alpha$  is the polarizability of the unit cell,  $V$  is the volume of the unit cell, and  $\epsilon_0$  is the dielectric constant.

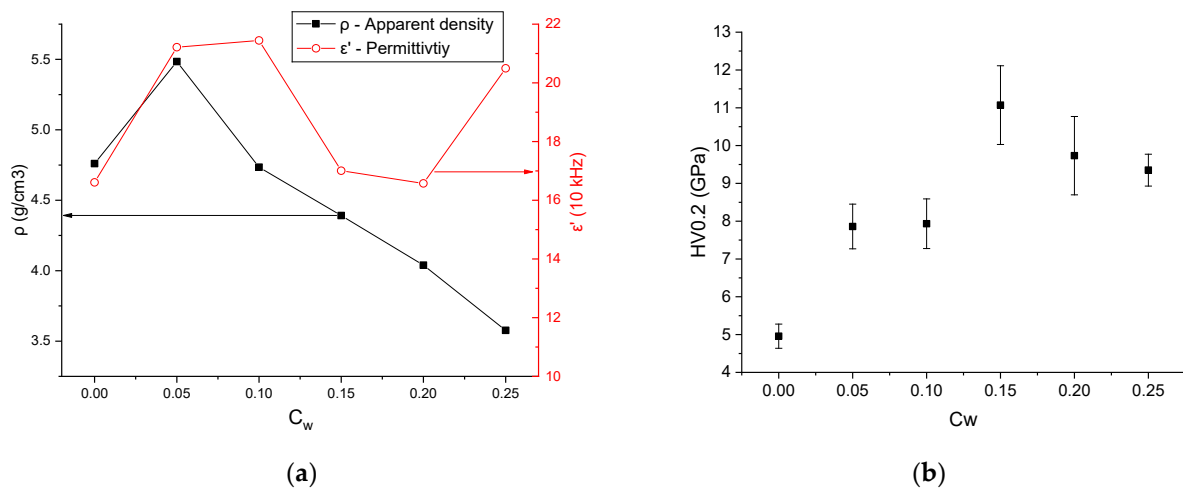


**Figure 8.** Dependences of apparent density and dielectric constant on mass concentration of dopant (a) and dependence of microhardness HV on dopant concentration (b).

In the case of the cubic lattice of  $ZrO_2\text{-}c$ , in addition to the volume reduction, an increase in the ionicity of the crystal bonding between the anions and cations can be assumed, which increases the polarizability  $\alpha$ . Then, according to Equation (1), there will be an increase in the dielectric permittivity. Similar behavior of dielectric properties in ceramics is observed for Y-stabilized  $ZrO_2$ , in which at low concentrations of yttrium

oxide, a sharp increase in the dielectric constant is observed; for crystals with tetragonal structures, an almost twofold increase is obtained [44,46]. At  $C_w = 0.15$  and  $C_w = 0.20$ , the determining factor in the dielectric permittivity is porosity, which can be seen from the curves in Figure 8. However, at the highest concentration of the dopant, the dielectric permittivity increases to 21, which is close to the maximum value for the series of the studied ceramics. This effect can be explained by the phase composition of the ceramics, which, according to Table 3, has a 64.58% cubic phase and a 34.42%  $\text{CaZrO}_3$  phase. Calcium zirconate has a perovskite structure with a non-centrosymmetric crystal lattice, which gives rise to a large dipole moment in the cell [47]. According to the effective medium theory, the dielectric constant of a heterogeneous medium is a function of the dielectric constant of the components and their concentrations [48]. Assuming that the dielectric constant of calcium zirconate is sufficiently high, an increase in its fraction can cause an increase in the dielectric constant despite the higher porosity of the synthesized ceramics. The dielectric permittivity of  $\text{CaZrO}_3$  is estimated to be 23–32 in a number of studies [49–51], which is greater than that of highly doped Ca-substituted zirconia ceramics [52].

Figure 8b shows the results of the Vickers microhardness measurements. The sample with a concentration of  $C_w = 0.15$  is characterized by high microhardness  $\text{HV}_{0.2} = 11.2$  GPa, which is comparable to other data in the literature on zirconia ceramics [53–55]. The microhardness and dielectric constant of ceramics depend on the phase composition and porosity. The grain size can also be emphasized as an additional factor that can affect the microhardness. In large grains, the propagation of mechanical stresses through dislocations occurs over long distances. In the case of small grains, dislocations stop at intergranular boundaries, making defect formation more difficult [56]. In other words, when the proportion of intergranular boundaries is large, the probability of crossing already formed dislocations of different orientations and crystal lattice types, which are contained in neighboring grains, increases. In this case, anchor points are created to prevent the atomic planes from sliding relative to each other. The low microhardness of the undoped sample can be explained by the presence of tensile stresses and microcracks in the structure after annealing. With increasing dopant concentration, the microhardness increased owing to the decrease in porosity at  $C_w = 0.05$  and the change in average grain size. For the samples with  $C_w = 0.10$  and  $C_w = 0.15$ , a significant decrease in density and an increase in grain size were observed compared to the sample with the lowest dopant fraction. It is also worth noting that in the case of these samples, the highest concentration of the cubic phase (more than 90%) was observed. Specifically, for the sample with a dopant concentration of 0.10, the highest values of average grain size and the percentage of grains with a size greater than  $12 \mu\text{m}$  (8%) were observed. For the sample with  $C_w = 0.15$ , the distribution histograms show that the percentage of grains with sizes larger than  $12 \mu\text{m}$  decreased to  $\sim 1\%$ . It can be concluded that the increase in microhardness in the obtained ceramics in the range of weight concentrations of 0.05–0.15  $\text{CaCO}_3$  is associated with the stabilization of the cubic phase and a narrower distribution of grain sizes. As the dopant concentration increased, the microhardness decreased, which was directly related to the decrease in the apparent density and the presence of a large number of pores in the microstructure. The formation of the  $\text{CaZrO}_3$  phase did not have a significant impact on the effective microhardness of the obtained samples because the microhardness values for  $\text{ZrO}_2$  and calcium zirconate were approximately the same.

#### 4. Conclusions

In this work, the phase composition and the electrical and mechanical properties of zirconia ceramics doped with  $\text{CaCO}_3$  at different weight concentrations ( $C_w = 0.05, 0.10, 0.15, 0.20$ , and  $0.25$ ) were investigated. After sintering in air at  $1500^\circ\text{C}$ , the obtained samples were two-phased, according to the known phase diagrams of the  $\text{ZrO}_2$ – $\text{CaO}$  system. With increasing dopant concentration, the following phase transformation was observed:  $\text{ZrO}_2\text{-m} \rightarrow \text{ZrO}_2\text{-m} + \text{ZrO}_2\text{-c}$  ( $C_w = 0.05\text{--}0.15$ )  $\rightarrow \text{ZrO}_2\text{-c} + \text{CaZrO}_3$  ( $C_w = 0.2\text{--}0.25$ ). The phase composition was also clarified using Raman spectroscopy, which showed the pres-

ence of the abovementioned phases. Using SEM, it was determined that increasing the concentration of  $\text{CaCO}_3$  significantly affected the morphology of the ceramics. With increasing  $C_w$ , a broadening of the measured grain size range was observed with increasing pore number. It can be stated that  $\text{CaCO}_3$  in the charge composition acts as a stabilizer of the cubic phase of  $\text{ZrO}_2$ , as well as a pore-forming agent. The features of the microstructure and phase composition directly affected the electrical and mechanical properties of the ceramics. The highest dielectric constant was observed for the sample with the lowest dopant fraction owing to the high apparent density of the ceramics. The obtained zirconia ceramic samples can be characterized as high-Q dielectrics with dielectric losses in the frequency region of 200–200 kHz  $\sim$  0.005 and dielectric constants of 16.4–22. The highest microhardness was observed for samples with the maximum fraction of the cubic phase and a narrower grain size distribution. Despite the high porosity of the resulting sample, using a cheaper reagent (calcium carbonate) in the solid-phase synthesis of high-content cubic zirconia ceramics turned out to be justified. All in all, a preliminary study of their mechanical and electrical properties and phase compositions showed that synthesized doped zirconia ceramics are applicable as inert matrices for next-generation nuclear dispersed fuel.

**Author Contributions:** Conceptualization, S.G.G., R.I.S., N.O.V., D.B.B., D.I.S. and A.L.K.; methodology, S.G.G., R.I.S., N.O.V., D.B.B., D.I.S. and A.L.K.; formal analysis, S.G.G., R.I.S., N.O.V., D.B.B., D.I.S. and A.L.K.; investigation, S.G.G., R.I.S., N.O.V., D.B.B., D.I.S. and A.L.K.; resources, S.G.G., R.I.S., N.O.V., D.B.B., D.I.S. and A.L.K.; writing—original draft preparation, review, and editing, S.G.G., R.I.S., N.O.V., D.B.B., D.I.S. and A.L.K.; visualization, S.G.G., R.I.S., N.O.V., D.B.B., D.I.S. and A.L.K.; supervision, S.G.G., R.I.S., N.O.V., D.B.B., D.I.S. and A.L.K. All authors have read and agreed to the published version of the manuscript.

**Funding:** This study was financially supported by the Science Committee of the Ministry of Science and Higher Education of the Republic of Kazakhstan (No. AP19679979).

**Institutional Review Board Statement:** Not applicable.

**Informed Consent Statement:** Not applicable.

**Data Availability Statement:** Not applicable.

**Conflicts of Interest:** The authors declare no conflict of interest.

## References

1. Mistarihi, Q.M.; Raj, V.; Kim, J.H.; Ryu, H.J. Thermal Conductivity of Mo-Reinforced  $\text{ZrO}_2$  Composites Fabricated by Spark Plasma Sintering for Inert Matrix Fuels. *Mater. Des.* **2017**, *134*, 476–485. [\[CrossRef\]](#)
2. Lemaignan, C.; Niepce, J. Chapter 13. Nuclear Ceramics: Fuels, Absorbers and Inert Matrices. In *Ceramic Materials: Processes, Properties and Applications*; Boch, P., Niepce, J., Eds.; John Wiley & Sons: Hoboken, NJ, USA, 2007. [\[CrossRef\]](#)
3. Matzke, H.; Rondinella, V.V.; Wiss, T. Materials Research on Inert Matrices: A Screening Study. *J. Nucl. Mater.* **1999**, *274*, 47–53. [\[CrossRef\]](#)
4. Nandi, C.; Grover, V.; Bhandari, K.; Bhattacharya, S.; Mishra, S.; Banerjee, J.; Prakash, A.; Tyagi, A.K. Exploring YSZ/ $\text{ZrO}_2$ - $\text{PuO}_2$  Systems: Candidates for Inert Matrix Fuel. *J. Nucl. Mater.* **2018**, *508*, 82–91. [\[CrossRef\]](#)
5. Kulyk, V.; Duriagina, Z.; Kostryzhev, A.; Vasylyv, B.; Marenych, O. Effects of Sintering Temperature and Yttria Content on Microstructure, Phase Balance, Fracture Surface Morphology, and Strength of Yttria-Stabilized Zirconia. *Appl. Sci.* **2022**, *12*, 11617. [\[CrossRef\]](#)
6. Sivaperumal, V.R.; Mani, R.; Poliseti, V.; Aruchamy, K.; Oh, T. Synthesis of Hydroxyapatite (HAp)-Zirconia Nanocomposite Powder and Evaluation of Its Biocompatibility: An In Vitro Study. *Appl. Sci.* **2022**, *12*, 11056. [\[CrossRef\]](#)
7. Chee Hon Cheong, A.; Sivanesan, S. The Application of Yttria-Stabilized Zirconia (YSZ). In *Zirconia—New Advances, Structure, Fabrication and Applications [Working Title]*; IntechOpen Limited: London, UK, 2023. [\[CrossRef\]](#)
8. Poznyak, A.; Pligovka, A.; Salerno, M. Anodizing of Hydrogenated Titanium and Zirconium Films. *Materials* **2021**, *14*, 7490. [\[CrossRef\]](#)
9. Garvie, R.C.; Hannink, R.H.; Pascoe, R.T. Ceramic Steel? In *Sintering Key Papers*; Springer: Dordrecht, The Netherlands, 1990; pp. 253–257. [\[CrossRef\]](#)
10. Chevalier, J.; Gremillard, L.; Virkar, A.V.; Clarke, D.R. The Tetragonal-Monoclinic Transformation in Zirconia: Lessons Learned and Future Trends. *J. Am. Ceram. Soc.* **2009**, *92*, 1901–1920. [\[CrossRef\]](#)
11. Arnold, B. *Zircon, Zirconium, Zirconia—Similar Names, Different Materials*; Springer: Berlin/Heidelberg, Germany, 2022; ISBN 978-3-662-64268-9.

12. Drazin, J.W.; Castro, R.H.R. Phase Stability in Nanocrystals: A Predictive Diagram for Yttria–Zirconia. *J. Am. Ceram. Soc.* **2015**, *98*, 1377–1384. [[CrossRef](#)]
13. Simpson, L.A.; Carter, R.E. Oxygen Exchange and Diffusion in Calcia-Stabilized Zirconia. *J. Am. Ceram. Soc.* **1966**, *49*, 139–144. [[CrossRef](#)]
14. Cales, B.; Baumard, J.F. Oxygen Semipermeability and Electronic Conductivity in Calcia-Stabilized Zirconia. *J. Mater. Sci.* **1982**, *17*, 3243–3248. [[CrossRef](#)]
15. Nakamura, A.; Wagner, J.B. Defect Structure, Ionic Conductivity, and Diffusion in Calcia-Stabilized Zirconia. *J. Electrochem. Soc.* **1980**, *127*, 2325–2333. [[CrossRef](#)]
16. Kumar, A.; Kumar, P.; Dhaliwal, A.S. Phase Transformation Behavior of Ca-Doped Zirconia Sintered at Different Temperatures. *J. Korean Ceram. Soc.* **2022**, *59*, 370–382. [[CrossRef](#)]
17. Kostishin, V.G.; Shakirzyanov, R.I.; Nalagin, A.G.; Shcherbakov, S.V.; Isaev, I.M.; Nemirovich, M.A.; Mikhailenko, M.A.; Korobeinikov, M.V.; Mezentseva, M.P.; Salogub, D.V. Electrical and Dielectric Properties of Yttrium–Iron Ferrite Garnet Polycrystals Grown by the Radiation–Thermal Sintering Technology. *Phys. Solid State* **2021**, *63*, 435–441. [[CrossRef](#)]
18. Isaev, I.M.; Kostishin, V.G.; Korovushkin, V.V.; Salogub, D.V.; Shakirzyanov, R.I.; Timofeev, A.V.; Mironovich, A.Y. Magnetic and Radio-Absorbing Properties of Polycrystalline  $\text{Li}_{0.33}\text{Fe}_{2.29}\text{Zn}_{0.21}\text{Mn}_{0.17}\text{O}_4$  Spinel Ferrite. *Tech. Phys.* **2021**, *66*, 1216–1220. [[CrossRef](#)]
19. Lira, C.; Fredel, M.C.; da Silveria, M.D.; Alarcon, O.E. Effect of Carbonates on Firing Shrinkage and on Moisture Expansion of Porous Ceramic Tiles. In Proceedings of the V. World Congress on Ceramic Tile Quality-Qualicer, Castellon, Spain, 8–11 March 1998; Volume 98, pp. 101–106. [[CrossRef](#)]
20. Aripin, H.; Priatna, E.; Dedi, D.; Sudiana, I.N.; Sabchevski, S. Characterization of Ceramic Membrane Based on Calcium Carbonate from Onyx Stone and Its Application for Coconut Sap Treatment. *Int. J. Eng.* **2022**, *35*, 300–306. [[CrossRef](#)]
21. Simão, L.; Montedo, O.R.K.; Caldato, R.F.; Innocentini, M.D.d.M.; Paula, M.M.d.S.; Angioletto, E.; Dal-Bó, A.G.; da Silva, L. Porous Ceramic Structures Obtained from Calcium Carbonate as Pore Generating Agent. *Mater. Sci. Forum* **2014**, *775–776*, 755–760. [[CrossRef](#)]
22. Kozlovskiy, A.L.; Borgekov, D.B.; Zdorovets, M.V.; Kenzhina, I.E.; Shlimas, D.I. Study of Radiation Damage Kinetics in Dispersed Nuclear Fuel on Zirconium Dioxide Doped with Cerium Dioxide. *J. Compos. Sci.* **2023**, *7*, 277. [[CrossRef](#)]
23. DIN EN ISO 6507-2:2018; Metallic Materials—Vickers Hardness Test—Part 2: Verification and Calibration of Testing Machines (ISO 6507-2:2018). DIN Deutsches Institut für Normung e.V.: Berlin, Germany, 2018.
24. ISO 14705:2016; Fine Ceramics (Advanced Ceramics, Advanced Technical Ceramics)—Test Method for Hardness of Monolithic Ceramics at Room Temperature. ISO: Geneva, Switzerland, 2016.
25. Yin, Y.; Xu, J.; Ji, M.; Li, L.; Chen, M. A Critical Review on Sintering and Mechanical Processing of 3Y-TZP Ceramics. *Ceram. Int.* **2023**, *49*, 1549–1571. [[CrossRef](#)]
26. Doebelin, N.; Kleeberg, R. Profex: A Graphical User Interface for the Rietveld Refinement programBGMN. *J. Appl. Crystallogr.* **2015**, *48*, 1573–1580. [[CrossRef](#)] [[PubMed](#)]
27. Boch, P. *Ceramic Materials: Processes, Properties and Applications*; Nièpce, J.-C., Ed.; John Wiley & Sons: Hoboken, NJ, USA, 2007; ISBN 978-1-905209-23-1.
28. Pang, E.L.; McCandler, C.A.; Schuh, C.A. Reduced Cracking in Polycrystalline  $\text{ZrO}_2\text{-CeO}_2$  Shape-Memory Ceramics by Meeting the Cofactor Conditions. *SSRN Electron. J.* **2019**, *177*, 230–239. [[CrossRef](#)]
29. Duwez, P.; Odell, F.; Brown, F.H. Stabilization of Zirconia with Calcia and Magnesia. *J. Am. Ceram. Soc.* **1952**, *35*, 107–113. [[CrossRef](#)]
30. Noguchi, T.; Mizuno, M.; Conn, W.M. Fundamental Research in Refractory System with a Solar Furnace— $\text{ZrO}_2$  CaO System. *Sol. Energy* **1967**, *11*, 145–152. [[CrossRef](#)]
31. Nath, D.; Singh, F.; Das, R. X-Ray Diffraction Analysis by Williamson–Hall, Halder–Wagner and Size–Strain Plot Methods of CdSe Nanoparticles—A Comparative Study. *Mater. Chem. Phys.* **2020**, *239*, 122021. [[CrossRef](#)]
32. Mokrushin, A.S.; Simonenko, E.P.; Simonenko, N.P.; Bukunov, K.A.; Sevastyanov, V.G.; Kuznetsov, N.T. Microstructure, Phase Composition, and Gas-Sensing Properties of Nanostructured  $\text{ZrO}_2\text{-xY}_2\text{O}_3$  Thin Films and Powders Obtained by the Sol-Gel Method. *Ionics* **2018**, *25*, 1259–1270. [[CrossRef](#)]
33. Tarrida, M.; Larguem, H.; Madon, M. Structural Investigations of  $(\text{Ca,Sr})\text{ZrO}_3$  and  $\text{Ca}(\text{Sn,Zr})\text{O}_3$  Perovskite Compounds. *Phys. Chem. Miner.* **2009**, *36*, 403–413. [[CrossRef](#)]
34. Rueden, C.T.; Schindelin, J.; Hiner, M.C.; DeZonia, B.E.; Walter, A.E.; Arena, E.T.; Eliceiri, K.W. ImageJ2: ImageJ for the next Generation of Scientific Image Data. *BMC Bioinform.* **2017**, *18*, 529. [[CrossRef](#)]
35. German, R.M. *Sintering Theory and Practice*; Wiley-VCH: Weinheim, Germany, 1996; ISBN 978-0-471-05786-4.
36. Burke, J.E.; Fulrath, R.M.; Pask, J.A. *Ceramic Microstructures*; John Wiley & Sons: New York, NY, USA, 1968; ISBN 978-0-471-28720-9.
37. Chauhan, L.; Shukla, A.K.; Sreenivas, K. Dielectric and Magnetic Properties of Nickel Ferrite Ceramics Using Crystalline Powders Derived from DL Alanine Fuel in Sol–Gel Auto-Combustion. *Ceram. Int.* **2015**, *41*, 8341–8351. [[CrossRef](#)]
38. Liu, P.; Yao, Z.; Zhou, J.; Yang, Z.; Kong, L.B. Small Magnetic Co-Doped NiZn Ferrite/Graphene Nanocomposites and Their Dual-Region Microwave Absorption Performance. *J. Mater. Chem. C* **2016**, *4*, 9738–9749. [[CrossRef](#)]
39. Tanriverdi, E.E.; Uzumcu, A.T.; Kavas, H.; Demir, A.; Baykal, A. Conductivity Study of Polyaniline-Cobalt Ferrite ( $\text{PANI-CoFe}_2\text{O}_4$ ) Nanocomposite. *Nano-Micro Lett.* **2011**, *3*, 99–107. [[CrossRef](#)]

40. Huang, X.; Wei, J.; Zhang, Y.; Qian, B.; Jia, Q.; Liu, J.; Zhao, X.; Shao, G. Ultralight Magnetic and Dielectric Aerogels Achieved by Metal–Organic Framework Initiated Gelation of Graphene Oxide for Enhanced Microwave Absorption. *Nano-Micro Lett.* **2022**, *14*, 107. [[CrossRef](#)]
41. Sivakumar, N.; Narayanasamy, A.; Ponpandian, N.; Govindaraj, G. Grain Size Effect on the Dielectric Behavior of Nanostructured  $\text{Ni}_{0.5}\text{Zn}_{0.5}\text{Fe}_2\text{O}_4$ . *J. Appl. Phys.* **2007**, *101*, 084116. [[CrossRef](#)]
42. Ctibor, P.; Petrášek, J.; Sedláček, J.; Neufuss, K. Dielectric Properties of  $\text{CaZrO}_3$  Coatings Made by Plasma Spraying and Bulks Fired by Spark Plasma Sintering. *Mater. Res. Bull.* **2020**, *124*, 110775. [[CrossRef](#)]
43. Gurevich, V.L.; Tagantsev, A.K. Intrinsic Dielectric Loss in Crystals. *Adv. Phys.* **1991**, *40*, 719–767. [[CrossRef](#)]
44. Thompson, D.P.; Dickins, A.M.; Thorp, J.S. The Dielectric Properties of Zirconia. *J. Mater. Sci.* **1992**, *27*, 2267–2271. [[CrossRef](#)]
45. Hannay, J.H. The Clausius-Mossotti Equation: An Alternative Derivation. *Eur. J. Phys.* **1983**, *4*, 141–143. [[CrossRef](#)]
46. Lanagan, M.T.; Yamamoto, J.K.; Bhalla, A.; Sankar, S.G. The Dielectric Properties of Yttria-Stabilized Zirconia. *Mater. Lett.* **1989**, *7*, 437–440. [[CrossRef](#)]
47. Acosta, M.; Novak, N.; Rojas, V.; Patel, S.; Vaish, R.; Koruza, J.; Rossetti, G.A.; Rödel, J.  $\text{BaTiO}_3$ -Based Piezoelectrics: Fundamentals, Current Status, and Perspectives. *Appl. Phys. Rev.* **2017**, *4*, 041305. [[CrossRef](#)]
48. Wang, M.; Pan, N. Predictions of Effective Physical Properties of Complex Multiphase Materials. *Mater. Sci. Eng. R Rep.* **2008**, *63*, 1–30. [[CrossRef](#)]
49. Lee, H.; Kim, J.R.; Lanagan, M.J.; Trolrier-McKinstry, S.; Randall, C.A. High-Energy Density Dielectrics and Capacitors for Elevated Temperatures:  $\text{Ca}(\text{Zr,Ti})\text{O}_3$ . *J. Am. Ceram. Soc.* **2013**, *96*, 1209–1213. [[CrossRef](#)]
50. Lee, W.S.; Su, C.Y.; Lee, Y.C.; Lin, S.P.; Yang, T. Effects of Dopant on the Dielectric Properties of  $\text{CaZrO}_3$  Ceramic Sintered in a Reducing Atmosphere. *Jpn. J. Appl. Phys.* **2006**, *45*, 5853. [[CrossRef](#)]
51. Xing, C.; Wang, J.; Li, J.; Shi, F. Precise Prediction of Dielectric Property for  $\text{CaZrO}_3$  Ceramic. *J. Adv. Dielectr.* **2018**, *08*, 1850029. [[CrossRef](#)]
52. Sanesi, M.; Cremante, G.; Pizzini, S.; Wagner, V. On the Dielectric Constant of Zirconia and Lime-Zirconia. *Z. Naturforschung A* **1971**, *26*, 159–164. [[CrossRef](#)]
53. Abyzov, A.M. Aluminum Oxide and Alumina Ceramics (Review). Part 1. Properties of  $\text{Al}_2\text{O}_3$  and Commercial Production of Dispersed  $\text{Al}_2\text{O}_3$ . *Refract. Ind. Ceram.* **2019**, *60*, 24–32. [[CrossRef](#)]
54. Amin, A.; Mumu, H.T.; Sarker, S.; Alam, Z.; Gafur, M.A. Effects of Sintering Temperature and Zirconia Content on the Mechanical and Microstructural Properties of  $\text{MgO}$ ,  $\text{TiO}_2$  and  $\text{CeO}_2$  Doped Alumina–Zirconia (ZTA) Ceramic. *J. Korean Ceram. Soc.* **2022**, *60*, 141–154. [[CrossRef](#)]
55. Alfahed, B.; Alayad, A. The Effect of Sintering Temperature on Vickers Microhardness and Flexural Strength of Translucent Multi-Layered Zirconia Dental Materials. *Coatings* **2023**, *13*, 688. [[CrossRef](#)]
56. Rejab, N.A.; Azhar, A.Z.A.; Ratnam, M.M.; Ahmad, Z.A. The Relationship between Microstructure and Fracture Toughness of Zirconia Toughened Alumina (ZTA) Added with  $\text{MgO}$  and  $\text{CeO}_2$ . *Int. J. Refract. Met. Hard Mater.* **2013**, *41*, 522–530. [[CrossRef](#)]

**Disclaimer/Publisher’s Note:** The statements, opinions and data contained in all publications are solely those of the individual author(s) and contributor(s) and not of MDPI and/or the editor(s). MDPI and/or the editor(s) disclaim responsibility for any injury to people or property resulting from any ideas, methods, instructions or products referred to in the content.